Journal of Materials Chemistry A

PAPER

View Article Online
View Journal | View Issue

Cite this: J. Mater. Chem. A, 2018, 6, 20076

Highly efficient overall water splitting driven by all-inorganic perovskite solar cells and promoted by bifunctional bimetallic phosphide nanowire arrays†

Lianbo Ma, ‡[a] Wenjun Zhang,‡[a] Peiyang Zhao,‡[a] Jia Liang,‡[a] Yi Hu,[a] Guoyin Zhu,[a] Renpeng Chen,[a] Zuoxiu Tie,*[a] Jie Liu [ab] and Zhong Jin *[a]

Received 21st August 2018
Accepted 17th September 2018

DOI: 10.1039/c8ta08116f

rsc.li/materials-a

Overall water splitting driven by a sustainable solar energy source has been recognized as a promising route to produce clean and renewable hydrogen fuel. However, its practical application is restricted by the low energy conversion efficiency and poor stability of photocatalysts. Herein, we report the realization of highly efficient overall water splitting promoted by bifunctional bimetallic phosphide ($Ni_{0.5}Co_{0.5}P$) nanowire arrays vertically grown on carbon paper ($Ni_{0.5}Co_{0.5}P$/CP) and driven by highly stable all-inorganic perovskite solar cells (PSCs). The $Ni_{0.5}Co_{0.5}P$/CP electrocatalysts can provide abundant active sites, high electrical conductivity, and good contact interface with the electrolyte, thus showing remarkable activity and great durability for both the hydrogen evolution reaction (HER) and oxygen evolution reaction (OER). The electrolyzer assembled with both the $Ni_{0.5}Co_{0.5}P$/CP anode and cathode can afford a current density of 10 mA cm^{-2} at only 1.61 V and allow consecutive water splitting. The all-inorganic PSCs based on a $CsPb_{0.9}Sn_{0.1}IBr_2$ light absorber and a nanocarbon electrode exhibit remarkable stability. When driven by all-inorganic PSCs, the electrolyzer delivers a high overall energy conversion efficiency (3.12%) and good long-term durability.

Introduction

Human society calls for renewable energy sources, such as solar and wind power, to substitute rapidly consumed and non-renewable fossil fuels. However, most of the renewable energies are intermittent, and their large-scale applications need the assistance of energy conversion and storage techniques.[1–4] Electrocatalytic water splitting can realize the production of chemical energy in the form of hydrogen fuel, which is regarded as a clean fuel for energy conversion systems, especially for hydrogen fuel cells.[5–7] For improving the efficiency of overall water splitting, the overpotential and stability of electrocatalysts need to be optimized.[8,9] To date, earth-abundant compounds, including transition metal sulfides,[10–18] nitrides,[19,20] carbides,[21,22] and phosphides,[23–25] have been extensively studied for the hydrogen evolution reaction (HER). Meanwhile, transition metal hydroxides[26,27] and oxides[28,29] have been explored for the oxygen evolution reaction (OER). However, the potential choices of bifunctional electrocatalysts with high activity and stability simultaneously for both the HER and OER are rare.[30] It is challenging to integrate the electrocatalytic HER and OER activities into a single architecture with rich exposed active sites, fast charge transport, and excellent durability.[31–33]

On the other hand, it is vital to look for economical and sustainable energy sources to serve as a power supply for overall water splitting.[34,35] In recent years, perovskite solar cells (PSCs) have emerged as a novel class of photoelectrical conversion devices that can effectively adsorb sunlight and generate electrical power with high power conversion efficiency (PCE).[36] The first report of PSC driven electrocatalytic water splitting was demonstrated by Luo's group in 2014, providing a promising route for hydrogen fuel production.[37] Although great progress has been achieved in recent years, the efficient utilization of PSC driven water splitting is still restricted by the instability of PSCs. It is expected that by coupling novel bifunctional electrocatalysts with high-performance PSCs, the water splitting electrolyzer can enable high efficiency conversion of solar energy to chemical fuels. Herein, we report the realization of overall water splitting with bifunctional bimetallic $Ni_{0.5}Co_{0.5}P$ nanowire array electrocatalysts vertically grown on carbon paper (CP) driven by highly stable all-inorganic PSCs. The all-inorganic PSCs with high stability are based on a $CsPb_{0.9}Sn_{0.1}IBr_2$ light absorber and a nanocarbon counter electrode, as described in our previous work.[38] The all-inorganic PSCs possess several advantages: (1) in-expensive costs, without the use of rare materials or noble metals;[30,31] (2) simple and easy

[a]Key Laboratory of Mesoscopic Chemistry of MOE, School of Chemistry and Chemical Engineering, Nanjing University, Nanjing, Jiangsu, 210023, China. E-mail: zxtie@nju.edu.cn; zhongjin@nju.edu.cn

[b]Department of Chemistry, Duke University, Durham, North Carolina, 27708, USA

† Electronic supplementary information (ESI) available. See DOI: 10.1039/c8ta08116f

‡ These authors contributed equally to this work.

fabrication processes;[37,39] (3) good long-term stability compared to traditional organic–inorganic hybrid PSCs. In electrochemical tests, the $Ni_{0.5}Co_{0.5}P$/CP electrocatalysts exhibit superior electrocatalytic activity and stability for both the HER and OER. When coupled with $CsPb_{0.9}Sn_{0.1}IBr_2$-based all-inorganic PSCs, the assembled $Ni_{0.5}Co_{0.5}P$/CP||$Ni_{0.5}Co_{0.5}P$/CP electrolyzer delivers remarkable electrochemical performances.

Experimental

Preparation of $Ni_{0.5}Co_{0.5}P$/CP

Carbon paper (CP) with a size of 1 × 2 cm^2 was first pre-treated by immersing into 1.0 M HNO_3 solution for 3 h, and then washed with deionized water several times. 20 mmol of NH_4F and 12 mmol of urea were dissolved in 80 mL of water under vigorous stirring for 10 min. Subsequently, 3 mmol of nickel chloride hexahydrate ($NiCl_2 \cdot 6H_2O$) and 3 mmol of cobalt chloride hexahydrate ($CoCl_2 \cdot 6H_2O$) were added into the above solution, and the mixture was stirred for another 3 h. After that, the resultant transparent solution was transferred into an autoclave, and then the pre-treated CP was added into the mixture. After heating at 120 °C for 8 h, the autoclave was cooled down to room temperature naturally, and the product was washed by ultrasonication in deionized water. To obtain the final product, the NiCo-precursor/CP and sodium hypophosphite (NaH_2PO_2) were put into a tube furnace with NaH_2PO_2 at the upstream. The furnace was then heated at 300 °C for 2 h under Ar atmosphere (100 sccm) with a ramping rate of 2 °C min^{-1}. As control samples, CoP/CP and NiP/CP were fabricated in the same way as $Ni_{0.5}Co_{0.5}P$/CP, but only used $CoCl_2 \cdot 6H_2O$ or $NiCl_2 \cdot 6H_2O$ as the source material, respectively.

Characterization

Field-emission scanning electron microscopy (SEM) images and elemental mapping profiles were collected on an FEI Nova NanoSEM-450 instrument. Transmission electron microscopy (TEM, JEM-2100) was performed on a JEOL JEM-2100F using an accelerating voltage of 200 kV. The powder X-ray diffraction (XRD) patterns were recorded with an X-ray diffractometer (Bruker D-8 Advance) using Cu Kα ($\lambda = 1.5406$ Å) radiation with a scanning rate of 6° min^{-1}. X-ray photoelectron spectra (XPS) were measured on a PHI-5000 VersaProbe X-ray photoelectron spectrometer using Al Kα X-ray radiation. The compositions of the products were examined by inductively coupled plasma-optical emission spectroscopy (ICP-OES, Optima 5300DV).

Electrochemical measurements

The electrochemical performances of the as-prepared samples were tested on a typical three-electrode setup using a CHI 760E electrochemical workstation (Chenhua Instruments, Shanghai) at room temperature. A KOH solution (1.0 M) was used as the electrolyte. For the HER and OER tests, the as-prepared CoP/CP, $Ni_{0.5}Co_{0.5}P$/CP and NiP/CP were employed as the working electrodes directly, while a calibrated saturated calomel electrode (SCE) and platinum foil were used as the reference and counter electrodes, respectively. For the overall water splitting measurements, two $Ni_{0.5}Co_{0.5}P$/CP electrodes were employed as the anode and cathode, respectively. Chronoamperometry measurement was conducted and linear sweep voltammetry (LSV) was performed at a scan rate of 2.0 mV s^{-1}. Moreover, the onset overpotential was defined as the potential at a current density of 0.5 mA cm^{-2}. A gas chromatograph (Agilent GC7890) was employed to analyze the volume of generated H_2 and O_2 during the electrochemical measurements.

Results and discussion

The synthesis steps of $Ni_{0.5}Co_{0.5}P$/CP are schematically illustrated in Fig. 1a and detailed in the Experimental section. Firstly, NiCo-precursor nanowire arrays were grown on the CP as an intermediate product (denoted as NiCo-precursor/CP) *via* a hydrothermal method. Subsequently, the NiCo-precursor/CP was put into a tube furnace with sodium hypophosphite (NaH_2PO_2) placed at the upstream. Through a mild heating treatment step under an Ar atmosphere, the NiCo-precursor nanowires were converted into bimetallic $Ni_{0.5}Co_{0.5}P$ nanowires, resulting in the formation of $Ni_{0.5}Co_{0.5}P$/CP. Fig. 1b shows the scanning electron microscopy (SEM) image of the NiCo-precursor/CP product, showing the nanowires grown vertically and homogeneously on the surfaces of carbon fibers. After phosphidation, the finally produced $Ni_{0.5}Co_{0.5}P$/CP well

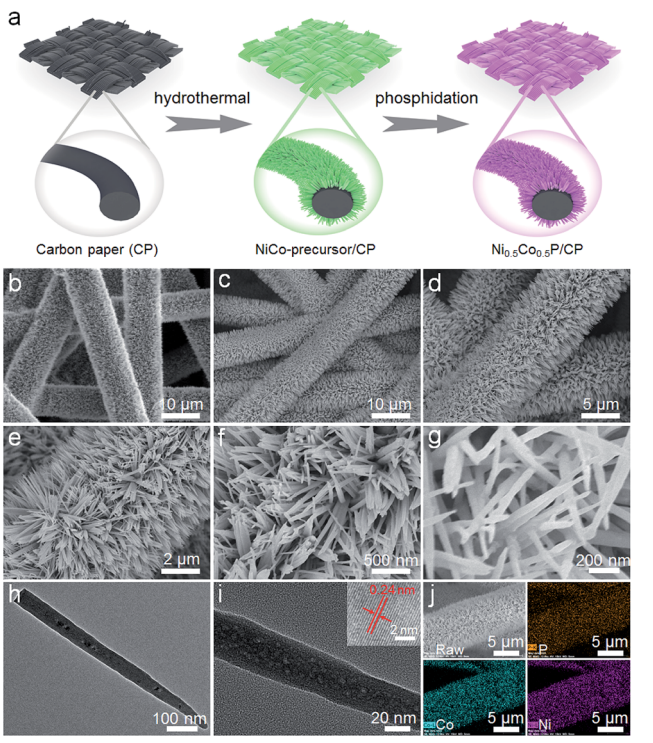

Fig. 1 Synthesis and structural characterization of $Ni_{0.5}Co_{0.5}P$/CP. (a) Schematic illustration of the synthesis process of $Ni_{0.5}Co_{0.5}P$/CP. (b) SEM image of the NiCo-precursor/CP as an intermediate product. (c–g) SEM images of the as-prepared $Ni_{0.5}Co_{0.5}P$/CP with different magnifications. (h and i) TEM images of the $Ni_{0.5}Co_{0.5}P$ nanowires grown on CP. The inset of (i) shows a HRTEM image of the $Ni_{0.5}Co_{0.5}P$ nanowire. (j) Elemental mappings of $Ni_{0.5}Co_{0.5}P$/CP.

retained the initial structure of NiCo-precursor/CP, and no structural collapse was observed (Fig. 1c). The void spaces between the nanowires (Fig. 1d and e) can efficiently facilitate the electrolyte diffusion and provide good contact interface with the electrolyte. Fig. 1f and g indicate that the $Ni_{0.5}Co_{0.5}P$ nanowires can reach several micrometers in length and have relatively smooth surface features. Transmission electron microscopy (TEM) characterization showed that the $Ni_{0.5}Co_{0.5}P$ nanowires possess a porous structure with abundant mesopores of several nanometers (Fig. 1h and i). Such a porous nanostructure can further promote the infiltration of the electrolyte and provide abundant active sites for electrocatalysis. High-resolution TEM (HRTEM, the inset of Fig. 1i) revealed an interlayer spacing of 0.24 nm, corresponding to the (111) planes of $Ni_{0.5}Co_{0.5}P$. The SEM image and the corresponding elemental mappings (Fig. 1j) indicate the co-existence and homogeneous distribution of P, Co and Ni elements in the $Ni_{0.5}Co_{0.5}P$ nanowires. As control samples, the SEM images of CoP/CP and NiP/CP are presented in Fig. S1.† It can be clearly seen that the CoP/CP exhibits morphological features similar to $Ni_{0.5}Co_{0.5}P$/CP, while the NiP/CP shows very different features with rough and porous nanoplates attached on the CP.

The crystalline structure and compositions of $Ni_{0.5}Co_{0.5}P$/CP and control samples were investigated. Besides the strong diffraction peak belonging to the CP at 26.5°, the XRD pattern of $Ni_{0.5}Co_{0.5}P$/CP (Fig. 2a) exhibits peak characteristics similar to that of CoP (JCPDS card, no. 29-0497). This indicates that the crystal structure of $Ni_{0.5}Co_{0.5}P$ is still analogous to CoP, as illustrated in the inset of Fig. 2a. While for NiP/CP (Fig. S2†), the XRD pattern reveals the existence of the CP and the typical diffraction peaks of NiP (JCPDS card, no. 18-0882). Fig. S3† shows the survey XPS spectrum of $Ni_{0.5}Co_{0.5}P$/CP. The molar ratio of Ni to Co is calculated to be close to 1 : 1, agreeing well with the initial feeding ratio of Ni to Co salts. The high-resolution XPS spectrum in the P 2p region is presented in Fig. 2b. It consists of two peaks at 130.2 and 129.1 eV, corresponding to the binding energies of P $2p_{1/2}$ and P $2p_{3/2}$, respectively, which are ascribed to the metal phosphides.[40] A broad peak at ~133.0 eV is assigned to the phosphate species resulting from the surface oxidation of $Ni_{0.5}Co_{0.5}P$ nanowires exposed to the air, consistent with those in the previous literature.[41–43] As regards to the Co 2p region (Fig. 2c), it shows two distinguished doublets located at a low energy band (Co $2p_{3/2}$) and a high energy band (Co $2p_{1/2}$), respectively. The binding energy difference between the two doublets is over 15 eV, suggesting the co-existence of Co^{2+} and Co^{3+}.[44] Fig. 2d displays the high-resolution XPS spectrum in the Ni 2p region. Two spin–orbit doublets can be deconvoluted by using the Gaussian fitting method, which are attributed to the characteristics of Ni^{2+} and Ni^{3+}, and two shake-up satellite peaks, respectively. The intense satellite peaks indicate that the majority of Ni elements in the final product is Ni^{2+} cations.[45]

The HER performances of $Ni_{0.5}Co_{0.5}P$/CP and control samples were investigated under alkaline conditions. Due to the free-standing characteristics, $Ni_{0.5}Co_{0.5}P$/CP can be directly used as a binder-free electrode for electrochemical tests. Before the electrochemical measurements, N_2 was bubbled to eliminate the dissolved O_2 in the electrolyte, and the electrodes were activated by sweeping the cyclic voltammetry (CV) curves at 0.02 mV s^{-1} for 30 min. Fig. 3a shows the linear sweep voltammogram (LSV) polarization curves of CoP/CP, $Ni_{0.5}Co_{0.5}P$/CP and NiP/CP in 1.0 M KOH aqueous solution at 2 mV s^{-1}. Both CoP/CP and NiP/CP electrodes exhibit inferior electrocatalytic activities with onset overpotentials of 75 and 110 mV, respectively. As a control sample, the electrochemical performance of the pristine CP was also investigated. As shown in Fig. S4a and b,† the pristine CP displays the interconnected network morphology with a clean and smooth surface, and exhibits a poor electrocatalytic activity for the HER, which can be certainly neglected. The mass activities of different catalysts were also calculated, as supplied in Fig. S5,† further indicating

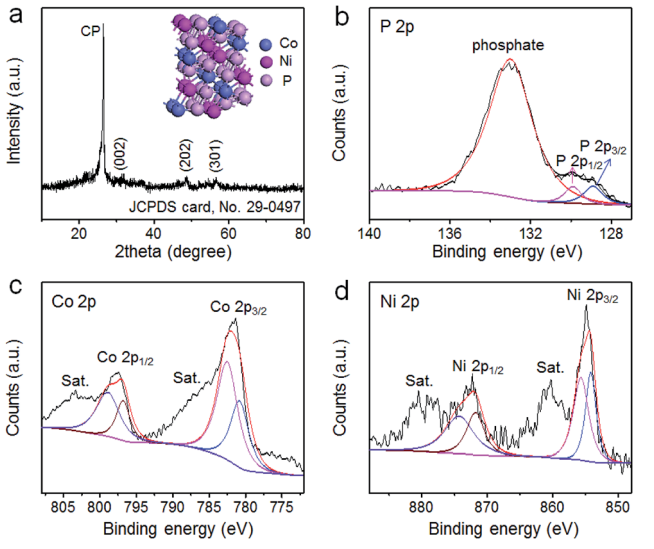

Fig. 2 Compositional characterization of $Ni_{0.5}Co_{0.5}P$/CP. (a) XRD pattern, (b–d) high-resolution XPS spectra at (b) P 2p, (c) Co 2p and (d) Ni 2p regions of $Ni_{0.5}Co_{0.5}P$/CP. The inset of (a) shows the crystalline structure configuration of $Ni_{0.5}Co_{0.5}P$.

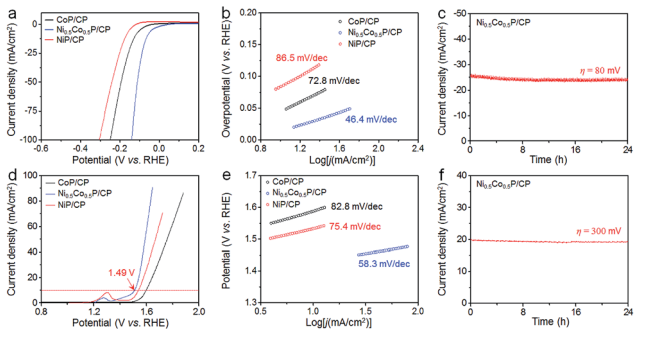

Fig. 3 HER and OER performances of CoP/CP, $Ni_{0.5}Co_{0.5}P$/CP and NiP/CP electrocatalysts in 1.0 M KOH solution. (a) LSV polarization curves and (b) the corresponding Tafel slopes of CoP/CP, $Ni_{0.5}Co_{0.5}P$/CP and NiP/CP. (c) Time-dependent current densities of $Ni_{0.5}Co_{0.5}P$/CP at a static overpotential of 80 mV. (d) LSV polarization curves and (e) the corresponding Tafel slopes of CoP/CP, $Ni_{0.5}Co_{0.5}P$/CP and NiP/CP. (f) Time-dependent current densities of $Ni_{0.5}Co_{0.5}P$/CP at a static overpotential of 300 mV.

the very high electrocatalytic activity of $Ni_{0.5}Co_{0.5}P$/CP. Moreover, CoP/CP and NiP/CP electrodes require large overpotentials of 123 and 174 mV, respectively, to afford a current density of 10 mA cm^{-2}. In contrast, $Ni_{0.5}Co_{0.5}P$/CP displays tremendously enhanced electrocatalytic activities after the introduction of both Ni and Co species. The $Ni_{0.5}Co_{0.5}P$/CP electrode shows the highest electrocatalytic activity with an onset overpotential around 10 mV, and a low overpotential of only 43 mV to achieve a current density of 10 mA cm^{-2}. Fig. S6a† shows the LSV polarization curve of the state-of-the-art Pt/C electrocatalyst, showing smaller onset overpotential value as compared with that of $Ni_{0.5}Co_{0.5}P$/CP. The Pt/C catalyst also needs a comparable overpotential of 38 mV to achieve a current density of 10 mA cm^{-2}. The corresponding Tafel slopes of these electrocatalysts were examined by fitting the linear portions of the Tafel plots in Fig. 3b, yielding the lowest Tafel slope of 46.4 mV dec^{-1} for $Ni_{0.5}Co_{0.5}P$/CP. According to the previous investigations on the HER mechanism in an alkaline solution,[11] such a low Tafel slope indicates that the HER process on the $Ni_{0.5}Co_{0.5}P$/CP electrode is much more facilitated than on others. Fig. S7a† shows the electrochemical impedance spectroscopy (EIS) plots of CoP/CP, $Ni_{0.5}Co_{0.5}P$/CP and NiP/CP electrocatalysts, revealing the comparable resistance characteristics with small values, indicating the fast electron transfer on this composite. Compared with the other reported electrocatalysts (Table S1†),[46–55] the $Ni_{0.5}Co_{0.5}P$/CP electrode exhibits much better electrocatalytic activity. As another important criterion, the electrochemical stability of $Ni_{0.5}Co_{0.5}P$/CP was evaluated by the time-dependent current density at a static overpotential of 80 mV. As shown in Fig. 3c, even after a long HER testing period (24 h), the current density of $Ni_{0.5}Co_{0.5}P$/CP remains almost unchanged, implying an ultrahigh stability.

Recently, transition metal phosphides have also shown great potential as electrocatalysts for the OER under alkaline conditions. In this regard, the OER performances of the samples were also examined. Fig. 3d shows the LSV polarization curves of CoP/CP, $Ni_{0.5}Co_{0.5}P$/CP and NiP/CP in 1.0 M KOH solution. Apparently, the $Ni_{0.5}Co_{0.5}P$/CP electrode delivers the highest catalytic activity among these samples. The achieved onset overpotential is only 240 mV, smaller than those of other samples (320 mV for CoP/CP and 270 mV for NiP/CP) and IrO_2 (260 mV, Fig. S6b†). The control sample of the pristine CP also shows a very poor electrocatalytic activity for the OER (Fig. S4c†), confirming that the pristine CP has almost no effect on the electrochemical performance of the metal phosphides/CP composites. Moreover, $Ni_{0.5}Co_{0.5}P$/CP needs an overpotential of only 260 mV to afford a current density of 10 mA cm^{-2}. A broad peak at about 1.30 V can be clearly observed from the LSV curve of $Ni_{0.5}Co_{0.5}P$/CP, which is attributed to the redox processes of the Ni species.[56,57] Based on the LSV polarization curves shown in Fig. 3d, the corresponding Tafel slopes were carefully calculated. As illustrated in Fig. 3e, the Tafel slopes of CoP/CP, $Ni_{0.5}Co_{0.5}P$/CP and NiP/CP are 82.8, 58.3 and 75.4 mV dec^{-1}, respectively. All the results indicate that $Ni_{0.5}Co_{0.5}P$/CP possesses the highest electrocatalytic activity for the OER among these samples. Moreover, the EIS plots of CoP/CP, $Ni_{0.5}Co_{0.5}P$/CP and NiP/CP electrocatalysts for the OER were also investigated (Fig. S7b†), further confirming the smooth electron transfer on these samples. In addition, compared with the other reported electrocatalysts, $Ni_{0.5}Co_{0.5}P$/CP also exhibits much better electrocatalytic activity (Table S2†),[58–67] further demonstrating the remarkable performance of $Ni_{0.5}Co_{0.5}P$/CP. The electrochemical stability of the $Ni_{0.5}Co_{0.5}P$/CP electrocatalysts for the OER was investigated. Fig. 3f shows the time-dependent current density of $Ni_{0.5}Co_{0.5}P$/CP under a static overpotential of 300 mV, showing remarkable stable current density in a long period time of 24 h.

Considering the excellent electrocatalytic activities of $Ni_{0.5}Co_{0.5}P$/CP for the HER and OER processes in alkaline solutions, an electrolyzer with a two-electrode configuration by employing $Ni_{0.5}Co_{0.5}P$/CP as both the anode and cathode for the overall water electrolysis was constructed (Fig. 4). Fig. 4a displays the polarization curves of the assembled electrolyzer, showing that the $Ni_{0.5}Co_{0.5}P$/CP||$Ni_{0.5}Co_{0.5}P$/CP electrode pair is able to catalyze the overall water splitting. As expected, the $Ni_{0.5}Co_{0.5}P$/CP||$Ni_{0.5}Co_{0.5}P$/CP couple delivers high electrochemical performance, and exhibits a current density of 10 mA cm^{-2} at only 1.61 V. This value is smaller than those of other reported bifunctional electrocatalysts (Table S3†).[33,34,68–72] The faradaic efficiencies of the $Ni_{0.5}Co_{0.5}P$/CP||$Ni_{0.5}Co_{0.5}P$/CP couple were investigated. As shown in Fig. 4b, the produced H_2 and O_2 measured quantitatively by the gas chromatography match well with the calculated amounts, and the molar ratio of H_2 : O_2 is close to 2.0, suggesting a high faradaic efficiency of ≈100%. Moreover, the electrochemical stability of the $Ni_{0.5}Co_{0.5}P$/CP||$Ni_{0.5}Co_{0.5}P$/CP couple was examined at 1.65 V. As revealed in Fig. 4c, the time-dependent current density shows excellent durability in long-term electrochemical measurements for

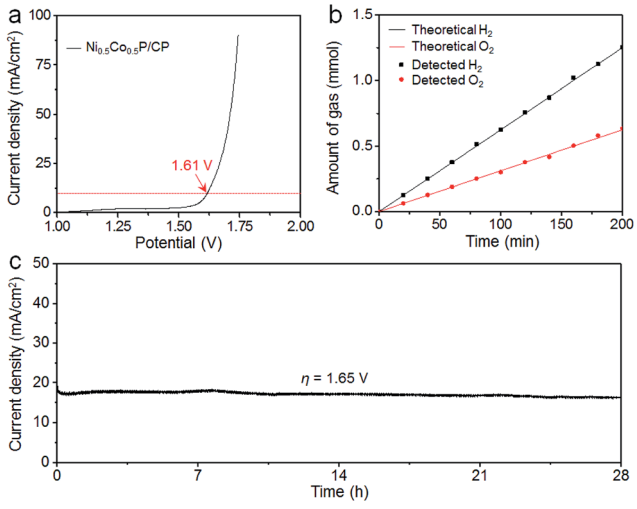

Fig. 4 Overall water splitting performance of the $Ni_{0.5}Co_{0.5}P$/CP electrocatalyst serving as both the anode and cathode in 1.0 M KOH solution. (a) LSV polarization curves of the overall water splitting system with the $Ni_{0.5}Co_{0.5}P$/CP||$Ni_{0.5}Co_{0.5}P$/CP configuration. (b) Comparison of the amounts of theoretically calculated and experimentally detected O_2 and H_2 generated from the $Ni_{0.5}Co_{0.5}P$/CP||$Ni_{0.5}Co_{0.5}P$/CP electrolyzer at a constant current density of 20 mA cm^{-2}. (c) Time-dependent current density of the $Ni_{0.5}Co_{0.5}P$/CP||$Ni_{0.5}Co_{0.5}P$/CP electrolyzer in 1.0 M KOH solution for 28 h.

about 28 h. In addition, the morphology of $Ni_{0.5}Co_{0.5}P$/CP was retained well after electrochemical testing for 28 h, as shown in Fig. S8,† suggesting the excellent stability and high structural integrity of $Ni_{0.5}Co_{0.5}P$/CP. Further tuning the relative ratios of Co to Ni to 1 : 2 and 2 : 1, the resultant catalysts (denoted as $Ni_{0.33}Co_{0.67}P$/CP and $Ni_{0.67}Co_{0.33}P$/CP) exhibit poorer catalytic activity, but with comparably high stability (Fig. S9†).

In addition, all-inorganic PSCs were employed to directly convert the sunlight to electrical energy for driving the overall water splitting, and $Ni_{0.5}Co_{0.5}P$/CP was used as the bifunctional electrocatalyst. Fig. 5a presents the configuration of the assembled electrolyzer, in which both the anode and cathode are composed of $Ni_{0.5}Co_{0.5}P$/CP, powered by the all-inorganic PSCs under simulated sunlight. The all-inorganic PSCs with exceptional stability are based on the $CsPb_{0.9}Sn_{0.1}IBr_2$ light absorber and the nanocarbon counter electrode, as detailed in our previous report.[38] The corresponding photovoltaic parameters, including short-circuit density (J_{sc}), open-circuit voltage (V_{oc}), fill factor (FF) and power conversion efficiency (PCE) of the all-inorganic PSCs are summarized in the inset of Fig. 5b, showing a PCE as high as 10.8%. The assembled electrolyzer can work well with two series-connected all-inorganic PSCs under simulated sunlight. The repeated current on-off cycles of the assembled electrolyzer were recorded, which are well consistent with the on-off periods of simulated sunlight (Fig. 5c). Moreover, the assembled electrolyzer exhibits good cycling stability with the current retention maintaining at 83.4% after 24 h (Fig. 5d). The overall water splitting driven by all-inorganic PSCs was also recorded by a real-time video (Video S1†). The inset of Fig. 5d shows the photograph of the electrolyzer working under simulated sunlight, showing clear O_2 and H_2 bubbles generated from the anode and cathode, respectively. Fig. S10† displays the amount of generated H_2 *versus* reaction time driven by all-inorganic PSCs. Combining with the PCE of all-inorganic PSCs, the overall energy conversion efficiency is calculated to be 3.12%. This value is relatively high compared to the existing photocatalysis systems in the literature (Table S4†),[73–78] suggesting the great potential of all-inorganic PSCs for overall water splitting.

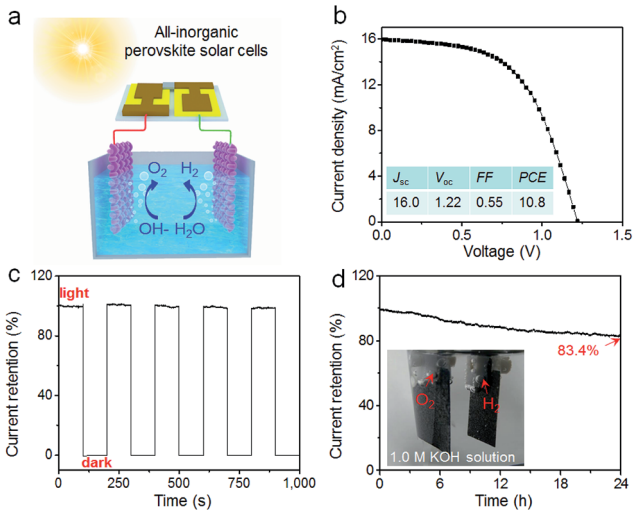

Fig. 5 Configuration and electrochemical performances of the assembled electrolyzer for overall water splitting. (a) Configuration of the electrolyzer with the $Ni_{0.5}Co_{0.5}P$/CP electrocatalyst serving as both the anode and cathode, powered by all-inorganic PSCs under simulated sunlight. (b) Current density–potential (J–V) curve of the all-inorganic PSCs under simulated AM 1.5G (100 mW cm^{-2}) illumination. The inset shows the corresponding photovoltaic parameters. (c) Chronoamperometric measurements of the solar energy-derived water electrolysis with/without the illumination of simulated sunlight. (d) Current density retention of the all-inorganic PSC-driven water splitting under continuous illumination for 24 h. The inset of (d) shows the photograph of the electrolyzer working under simulated sunlight, and the red arrows indicate the generation of H_2 and O_2 bubbles.

Conclusions

In summary, bifunctional $Ni_{0.5}Co_{0.5}P$/CP electrocatalysts coupled with all-inorganic PSCs were developed for solar-driven overall water splitting. With the merits of hierarchical and porous nanostructures of $Ni_{0.5}Co_{0.5}P$ nanowire arrays as well as the high electric conductivity provided by CP, the $Ni_{0.5}Co_{0.5}P$/CP can exhibit significantly enhanced electrocatalytic activity for H_2 and O_2 evolution at low overpotentials. The assembled electrolyzer with $Ni_{0.5}Co_{0.5}P$/CP serving as both the anode and cathode delivers stable electrocatalytic performance for overall water splitting over long periods of time. When coupled with all-inorganic PSCs, the assembled electrolyzer enables overall water splitting under simulated sunlight with a high overall energy conversion efficiency. The combination of low-cost and highly-active bimetallic phosphide electrocatalysts with highly stable all-inorganic PSCs allows the effective utilization of solar energy for overall water splitting.

Conflicts of interest

There are no conflicts to declare.

Acknowledgements

This work is supported by the National Key R&D Program of China (2017YFA0208200, 2016YFB0700600, 2015CB659300), the Projects of NSFC (21872069, 51761135104, 21573108), the Natural Science Foundation of Jiangsu Province (BK20150583, BK20160647, BK20180008), the High-Level Entrepreneurial and Innovative Talents Program of Jiangsu Province, and the Fundamental Research Funds for the Central Universities (020514380146).

Notes and references

1 M. G. Walter, E. L. Warren, J. R. McKone, S. W. Boettcher, Q. X. Mi, E. A. Santori and N. S. Lewis, *Chem. Rev.*, 2010, **110**, 6446–6473.
2 W. H. Zuo, W. H. Zhu, D. F. Zhao, Y. F. Sun, Y. Y. Li, J. P. Liu and X. W. (David) Lou, *Energy Environ. Sci.*, 2016, **9**, 2881–2891.
3 C. Wang, L. X. Wu, H. Wang, W. H. Zuo, Y. Y. Li and J. P. Liu, *Adv. Funct. Mater.*, 2015, **25**, 3524–3533.

4 R. Z. Li, Y. M. Wang, C. Zhou, C. Wang, X. Ba, Y. Y. Li, X. T. Huang and J. P. Liu, *Adv. Funct. Mater.*, 2015, **25**, 5384–5394.
5 Z. P. Shao and S. M. Haile, *Nature*, 2004, **431**, 170–173.
6 A. C. Dillon, K. M. Jones, T. A. Bekkedahl, C. H. Kiang, D. S. Bethune and M. J. Heben, *Nature*, 1997, **386**, 377–379.
7 R. Bashyam and P. Zelenay, *Nature*, 2006, **443**, 63–66.
8 X. Zou and Y. Zhang, *Chem. Soc. Rev.*, 2015, **44**, 5148–5180.
9 D. Voiry, H. Yamaguchi, J. Li, R. Silva, D. C. B. Alves, T. Fujita, M. Chen, T. Asefa, V. B. Shenoy, G. Eda and M. Chhowalla, *Nat. Mater.*, 2013, **12**, 850–855.
10 L. B. Ma, Y. Hu, G. Y. Zhu, R. P. Chen, T. Chen, H. L. Lu, Y. R. Wang, J. Liang, H. X. Liu, C. Z. Yan, Z. X. Tie, Z. Jin and J. Liu, *Chem. Mater.*, 2016, **28**, 5733–5742.
11 L. B. Ma, Y. Hu, R. P. Chen, G. Y. Zhu, T. Chen, H. L. Lv, Y. R. Wang, J. Liang, H. X. Liu, C. Z. Yan, H. F. Zhu, Z. X. Tie, Z. Jin and J. Liu, *Nano Energy*, 2016, **24**, 139–147.
12 M. A. Lukowski, A. S. Daniel, C. R. English, F. Meng, A. Forticaux, R. J. Hamers and S. Jin, *Energy Environ. Sci.*, 2014, **7**, 2608–2613.
13 X. Y. Yu, L. Yu, H. B. Wu and X. W. Lou, *Angew. Chem., Int. Ed.*, 2015, **54**, 5331–5335.
14 L. Wang, X. Luo, J. Luo, X. Duan, J. Crittenden, C. Liu, S. Zhang, Y. Pei, Y. Zeng and X. Duan, *Angew. Chem., Int. Ed.*, 2017, **56**, 7610–7614.
15 C. B. Liu, L. L. Wang, Y. H. Tang, S. L. Luo, Y. T. Liu, S. Q. Zhang, Y. X. Zeng and Y. Z. Xu, *Appl. Catal., B*, 2015, **164**, 1–9.
16 L. L. Wang, X. D. Duan, G. M. Wang, C. B. Liu, S. L. Luo, S. Q. Zhang, Y. X. Zeng, Y. Z. Xu, Y. T. Liu and X. F. Duan, *Appl. Catal., B*, 2016, **186**, 88–96.
17 Y. Z. Xu, L. L. Wang, X. Liu, S. Q. Zhang, C. B. Liu, D. F. Yan, Y. X. Zeng, Y. Pei, Y. T. Liu and S. L. Luo, *J. Mater. Chem. A*, 2016, **4**, 16524–16530.
18 S. Zhang, X. Liu, S. Luo, L. Wang, T. Cai, Y. Zeng, J. Yuan, W. Dong, Y. Pei and Y. Liu, *ACS Nano*, 2018, **12**, 751–758.
19 W. F. Chen, K. Sasaki, C. Ma, A. I. Frenkel, N. Marinkovic, J. T. Muckerman, Y. M. Zhu and R. R. Adzic, *Angew. Chem., Int. Ed.*, 2012, **51**, 6131–6135.
20 M. Nagai, Y. Goto, O. Uchino and S. Omi, *Catal. Today*, 1998, **45**, 335–340.
21 L. B. Ma, X. P. Shen, J. Zhu, G. X. Zhu and Z. Y. Ji, *J. Mater. Chem. A*, 2015, **3**, 11066–11073.
22 S. Wang, J. Wang, M. Zhu, X. Bao, B. Xiao, D. Su, H. Li and Y. Wang, *J. Am. Chem. Soc.*, 2015, **137**, 15753–15759.
23 C. Tang, R. Zhang, W. B. Lu, L. B. He, X. Jiang, A. M. Asiri and X. P. Sun, *Adv. Mater.*, 2017, **29**, 1602441.
24 H. Wang, S. X. Min, Q. Wang, D. B. Li, G. Casillas, C. Ma, Y. G. Li, Z. X. Liu, L. J. Li, J. Y. Yuan, M. Antonietti and T. Wu, *ACS Nano*, 2017, **11**, 4358–4364.
25 E. J. Popczun, J. R. McKone, C. G. Read, A. J. Biacchi, A. M. Wiltrout, N. S. Lewis and R. E. Schaak, *J. Am. Chem. Soc.*, 2013, **135**, 9267–9270.
26 W. T. Hong, M. Risch, K. A. Stoerzinger, A. Grimaud, J. Suntivich and Y. Shao-Horn, *Energy Environ. Sci.*, 2015, **8**, 1404–1427.
27 X. Hu, F. Cheng, N. Zhang, X. Han and J. Chen, *Small*, 2015, **11**, 5545–5550.
28 F. X. Ma, H. B. Wu, B. Y. Xia, C. Y. Xu and X. W. Lou, *Angew. Chem., Int. Ed.*, 2015, **54**, 15395–15399.
29 D. Kong, H. Wang, Z. Lu and Y. Cui, *J. Am. Chem. Soc.*, 2014, **136**, 4897–4900.
30 M. Kuang, P. Han, Q. H. Wang, J. Li and G. F. Zheng, *Adv. Funct. Mater.*, 2016, **26**, 8555–8561.
31 A. Sivanantham, P. Ganesan and S. Shanmugam, *Adv. Mater.*, 2016, **26**, 4661–4672.
32 Z. X. Yin, C. L. Zhu, S. Zhang, X. T. Zhang and Y. J. Chen, *Nanoscale*, 2016, **8**, 19129–19138.
33 J. H. Song, C. Z. Zhu, B. Z. Xu, S. F. Fu, M. H. Engelhard, E. F. Ye, D. Du, S. P. Beckman and Y. H. Lin, *Adv. Energy Mater.*, 2016, **10**, 1601555.
34 B. Yu, N. Jiang, M. L. Sheng, S. Gul, J. Yano and Y. J. Sun, *Chem. Mater.*, 2015, **27**, 7636–7642.
35 Y. Y. Wu, G. D. Li, Y. P. Liu, L. Yang, X. R. Lian, T. Asefa and X. X. Zou, *Adv. Funct. Mater.*, 2016, **26**, 4839–4847.
36 B. Saparov and D. B. Mitzi, *Chem. Rev.*, 2016, **116**, 4558–4596.
37 J. S. Luo, J. H. Im, M. T. Mayer, M. Schreier, M. K. Nazeerudin, N. G. Park, S. D. Tilley, H. J. Fan and M. Gratzel, *Science*, 2014, **345**, 1593–1596.
38 J. Liang, P. Y. Zhao, C. X. Wang, Y. R. Wang, Y. Hu, G. Y. Zhu, L. B. Ma, J. Liu and Z. Jin, *J. Am. Chem. Soc.*, 2017, **139**, 14009–14012.
39 A. R. Bin, M. Yusoff and J. Jang, *Chem. Commun.*, 2016, **52**, 5824–5827.
40 J. Yu, Q. Q. Li, Y. Li, C. Y. Xu, L. Zhen, V. P. Dravid and J. S. Wu, *Adv. Funct. Mater.*, 2016, **26**, 7644–7651.
41 R. Ye, P. Angel-Vicente, Y. Liu, M. J. Arellano-Jimenez, Z. Peng, T. Wang, Y. Li, B. I. Yakobson, S. H. Wei, M. J. Yacaman and J. M. Tour, *Adv. Mater.*, 2016, **28**, 1427–1432.
42 R. Zhang, X. X. Wang, S. J. Yu, T. Wen, X. W. Zhu, F. X. Yang, X. N. Sun, X. K. Wang and W. P. Hu, *Adv. Mater.*, 2017, **29**, 1605502.
43 H. W. Huang, C. Yu, C. T. Zhao, X. T. Han, J. Yang, Z. B. Liu, S. F. Li, M. D. Zhang and J. S. Qiu, *Nano Energy*, 2017, **34**, 472–480.
44 J. Xu, P. Gao and T. S. Zhao, *Energy Environ. Sci.*, 2012, **5**, 5333–5339.
45 X. H. Xiong, G. Waller, D. Ding, D. C. Chen, B. Rainwater, B. Zhao, Z. X. Wang and M. L. Liu, *Nano Energy*, 2015, **16**, 71–80.
46 J. Q. Tian, Q. Liu, A. M. Asiri and X. P. Sun, *J. Am. Chem. Soc.*, 2014, **136**, 7587–7590.
47 D. N. Liu, Q. Lu, Y. L. Luo, X. P. Sun and A. M. Asiri, *Nanoscale*, 2015, **7**, 15122–15126.
48 X. J. Fan, H. Q. Zhou and X. Guo, *ACS Nano*, 2015, **9**, 5125–5134.
49 L. M. Lang, Y. Shi, J. Wang, F. B. Wang and X. H. Xia, *ACS Appl. Mater. Interfaces*, 2015, **7**, 9098–9102.
50 J. L. Shi, Z. H. Pu, Q. Liu, A. M. Asiri, J. M. Hu and X. P. Sun, *Electrochim. Acta*, 2015, **154**, 345–351.
51 J. Wang, H. X. Zhong, Z. L. Wang, F. L. Meng and X. B. Zhang, *ACS Nano*, 2016, **10**, 2342–2348.

52 Y. Feng, X. Y. Yu and U. Paik, *Chem. Commun.*, 2016, **52**, 1633–1636.
53 X. Zhang, H. M. Xu, X. X. Li, Y. Y. Li, T. B. Yang and Y. Y. Liang, *ACS Catal.*, 2016, **6**, 580–588.
54 J. M. McEnaney, T. L. Soucy, J. M. Hodges, J. F. Callejas, J. S. Mondschein and R. E. Schaal, *J. Mater. Chem. A*, 2016, **4**, 3077–3081.
55 H. B. Zhang, Z. J. Ma, J. J. Duan, H. M. Liu, G. G. Liu, T. Wang, K. Chang, M. Li, L. Shi, X. G. Meng, K. C. Wu and J. H. Ye, *ACS Nano*, 2016, **10**, 684–694.
56 Z. Huang, Z. Chen, Z. Chen, C. Lv, M. G. Humphrey and C. Zhang, *Nano Energy*, 2014, **9**, 373–382.
57 L. A. Stern, L. Feng, F. Song and X. Hu, *Energy Environ. Sci.*, 2015, **8**, 2347–2351.
58 Y. H. Dou, T. Liao, Z. Q. Ma, D. L. Tian, Q. N. Liu, F. Xiao, Z. Q. Sun, J. H. Kim and S. X. Dou, *Nano Energy*, 2016, **30**, 267–275.
59 B. L. Chen, G. P. Ma, Y. Q. Zhu, J. B. Wang, W. Xiong and Y. D. Xia, *J. Power Sources*, 2016, **334**, 112–119.
60 C. Yu, Z. B. Liu, X. T. Han, H. W. Huang, C. T. Zhao, J. Yang and J. S. Qiu, *Carbon*, 2016, **110**, 1–7.
61 Z. H. Xia, X. B. Huang, L. Xu, D. F. Yan, J. Huo and S. Y. Wang, *Chem. Commun.*, 2016, **52**, 13008–13011.
62 Q. C. Dong, Q. Wang, Z. Y. Dai, H. J. Qiu and X. C. Dong, *ACS Appl. Mater. Interfaces*, 2016, **8**, 26902–26907.
63 T. R. Zhan, Y. M. Zhang, X. L. Liu, S. S. Lu and W. G. Hou, *J. Power Sources*, 2016, **333**, 53–60.
64 S. H. Bae, J. Kim, H. Randriamahazaka, S. Y. Moon, J. Park and I. Oh, *Adv. Energy Mater.*, 2016, **7**, 1601492.
65 R. P. Antony, A. K. Satpati, K. Bhattacharyya and B. N. Jagatap, *Adv. Mater. Interfaces*, 2016, **3**, 1600632.
66 M. S. Balogun, W. T. Qiu, H. Yang, W. J. Fan, Y. C. Huang, P. P. Fang, G. R. Li, H. B. Ji and Y. X. Tong, *Energy Environ. Sci.*, 2016, **9**, 3411–3416.
67 Z. Y. Wang, J. T. Li, X. C. Tian, X. P. Wang, Y. Yu, K. S. Owusu, L. He and L. Q. Mai, *ACS Appl. Mater. Interfaces*, 2016, **8**, 19386–19392.
68 M. Ledendecker, S. Krick Calderón, C. Papp, H. P. Steinrck, M. Antonietti and M. Shalom, *Angew. Chem., Int. Ed.*, 2015, **127**, 12538–12542.
69 C. C. Sun, Q. C. Dong, J. Yang, Z. Y. Dai, J. J. Lin, P. Chen, W. Huang and X. C. Dong, *Nano Res.*, 2016, **9**, 2234–2243.
70 K. D. Li, J. F. Zhang, R. Wu, Y. F. Yu and B. Zhang, *Adv. Sci.*, 2016, **3**, 1500426.
71 X. H. Gao, H. X. Zhang, Q. G. Li, X. G. Yu, Z. L. Hong, X. W. Zhang, C. D. Liang and Z. Lin, *Angew. Chem., Int. Ed.*, 2016, **55**, 6290–6294.
72 Z. H. Pu, Y. L. Luo, A. M. Asiri and X. P. Sun, *ACS Appl. Mater. Interfaces*, 2016, **8**, 4718–4723.
73 C. Yan, X. Xue, W. Zhang, X. Li, J. Liu, S. Yang, Y. Hu, R. Chen, Y. Yan, G. Zhu, Z. Kang, D. Kang, J. Liu and Z. Jin, *Nano Energy*, 2017, **39**, 539–545.
74 M. Ebaid, D. Priante, G. Liu, C. Zhao, M. S. Alias, U. Buttner, T. K. Ng, T. T. Isimjan, H. Idriss and B. S. Ooi, *Nano Energy*, 2017, **37**, 158–167.
75 Y. J. Ma, Y. Liu, Y. Bian, A. Q. Zhu, Y. Yang and J. Pan, *J. Colloid Interface Sci.*, 2018, **518**, 140–148.
76 X. J. Guan, F. A. Chowdhury, N. Pant, L. J. Guo, L. Vayssieres and Z. T. Mi, *J. Phys. Chem. C*, 2018, **122**, 13797–13802.
77 Q. Wang, T. Hisatomi, Q. X. Jia, H. Tokudome, M. Zhong, C. Z. Wang, Z. H. Pan, T. Takata, M. Nakabayashi, N. Shibata, Y. B. Li, I. D. Sharp, A. Kudo, T. Yamada and K. Domen, *Nat. Mater.*, 2016, **15**, 611–615.
78 M. Schroder, K. Kailasam, J. Borgmeyer, M. Neumann, A. Thomas, R. Schomacker and M. Schwarze, *Energy Technol.*, 2015, **3**, 1014–1017.